7

Light Localization by Defects in Optically Induced Photonic Structures

Jianke Yang[1], Xiaosheng Wang[2], Jiandong Wang[1], and Zhigang Chen[2,3]

[1] Department of Mathematics and Statistics, University of Vermont, VT 05401, USA
jyang@cems.uvm.edu, jwang@cems.uvm.edu
[2] Department of Physics and Astronomy, San Francisco State University, CA 94132, USA
gxkren@gmail.com, zchen@stars.sfsu.edu
[3] TEDA Applied Physical School, Nankai University, Tianjin 300457, China

7.1 Introduction

In the past ten years, there has blossomed an interest in the study of collective behavior of wave propagation in periodic waveguide arrays and photonic lattices [1–3]. The unique bandgap structures of these periodic media, coupled with nonlinear effects, give rise to many types of novel soliton structures [1–26]. On the other hand, it is well known that one of the unique and most interesting features of photonic band-gap structures is a fundamentally different way of waveguiding by defects in otherwise uniformly periodic structures. Such waveguiding has been demonstrated with an "air-hole" in photonic crystal fibers (PCF) for optical waves [27, 28], in an isolated defect in two-dimensional arrays of dielectric cylinders for microwaves [29–31], and recently in all-solid PCF with a lower-index core [32, 33]. In addition, laser emission based on photonic defect modes has been realized in a number of experiments [34–38]. In one-dimensional (1D) fabricated semiconductor waveguide arrays, previous experiments have investigated nonlinearity-induced escape from a defect state [39] and interactions of discrete solitons with structural defects [40] (see also [41]).

Despite the above efforts, theoretical understanding on defect guiding was still limited, and experimental demonstrations of defect guiding was still scarce. In addition, when nonlinear effects are significant, how defect guiding is affected by nonlinearity is largely an open issue. Recently, in a series of theoretical and experimental studies, we optically induced 1D, 2D and ring-like photonic lattices with single-site negative defects in photorefractive crystals, and investigated their linear and nonlinear light guiding properties [42–48]. This work will be reviewed in this Chapter. In addition, we present the first experimental demonstration of nonlinear defect modes which undergoes nonlinear

propagation through the defects. Our work not only has a direct link to technologically important systems of periodic structures such as PCF, but also brings about the possibility for studying, in an optical setting, many novel phenomena in periodic systems beyond optics such as edge dislocation, defect healing, eigenmode splitting, and nonlinear mode coupling which have been intriguing scientists for decades [49–51].

7.2 Optically Induced Lattices and Defects

With today's nano-fabrication technology, creation of a closely-spaced uniform 1D waveguide array on a substrate material is not a difficult task. For instance, such waveguides have been fabricated with AlGaAs semiconductor materials or $LiNbO_3$ crystals. Yet, it has been a challenge to create or fabricate 2D or 3D waveguide arrays in bulk media. In Ref. [9], 2D photonic lattices were successfully created by sending multiple interfering beams into a crystal. This interference method has some disadvantages, such as its sensitivity to ambient perturbation, and its inability to generate more complicated lattice structures with single-site defects. In view of that, we used a different method of optical induction which is based on the amplitude modulation of a partially coherent optical beam.

The experimental setup for our study is illustrated in Fig. 7.1. The experiments are performed in a biased SBN:60 (strontium barium niobate) photorefractive crystal (typically, $r_{33} \sim 280\,\text{pm/V}$ and $r_{13} \sim 24\,\text{pm/V}$) illuminated by a laser beam (either Coherent argon ion laser $\lambda = 488\,\text{nm}$ or solid-state laser $\lambda = 532\,\text{nm}$) passing through a rotating diffuser and an amplitude mask. The biased crystal (bias field can be varied from -2.0 to 6.0 kV/cm) provides

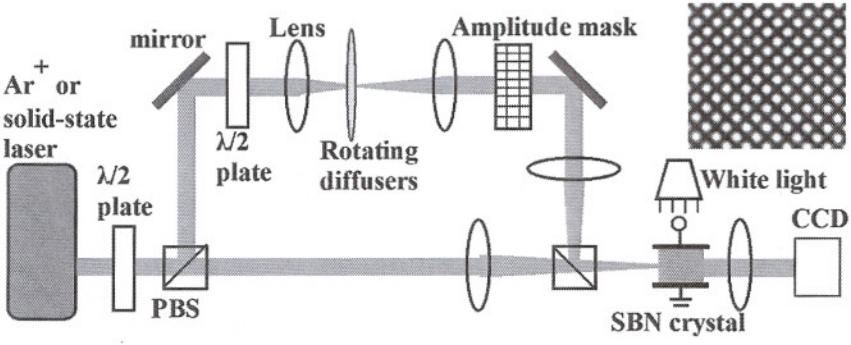

Fig. 7.1. Experimental setup for optical induction of waveguide lattices in a biased photorefractive crystal by amplitude modulation of a partially coherent beam. PBS: polarizing beam splitter, SBN: strontium barium niobate. Top path is the lattice beam, and bottom path is the probe beam (either a Gaussian beam or a vortex beam if a vortex mask is inserted). The right insert shows a typical experimental picture of 2D uniform lattice created by optical induction

a self-focusing or defocusing noninstantaneous nonlinearity [52]. The rotating diffuser turns the laser beam into a partially spatially incoherent beam with controllable degree of spatial coherence, as first introduced in experiments with incoherent optical solitons [53–55]. The amplitude mask provides spatial modulation after the diffuser on the otherwise uniform beam, which exhibits a periodic intensity pattern at the input face of the crystal [56,57]. This partially coherent and spatially modulated beam is used as our lattice beam. Another beam, either split from the same laser or emitted from a different laser and not passing through the diffuser and the mask, is used as our probe beam, propagating along with the lattice. In our experiments on defect modes, the lattice beam has its polarization close to being o-polarized, thus the lattice beam induces a weak periodic index variation to form the waveguide arrays. The probe beam, on the other hand, is always a coherent e-polarized beam, but its intensity and/or wavelength can be adjusted so it can undergo linear propagation (for study of linear guidance or linear defect modes) or nonlinear propagation (for study of nonlinear trapping or nonlinear defect modes) as detailed in later sections. The two beams are monitored separately with CCD cameras at the input and output facets of the crystal. In addition, a white-light background beam illuminating from the top of the crystal is normally used for fine-tuning the photorefractive nonlinearity [52–60].

In our experiments, the periodic lattice must stay stationary during its quasi-linear propagation through the crystal. In order for this to happen, we need to understand how to eliminate the *Talbot effect*. The Talbot effect is a phenomenon of coherent light propagation in a homogeneous media with spatially-periodic initial conditions [61,62]. Light exhibiting this phenomenon does not propagate stationarily, and it shrinks and expands as it moves along, and its intensity pattern repeats itself periodically along the propagation direction. Our lattice beam travels in a homogeneous crystal (as it does not feel the probe beam), and its initial condition on the input face of the crystal is periodic (due to the amplitude mask). Because of the Talbot effect, it can not form a stationary lattice. To overcome this difficulty, our idea is to use frequency filtering to remove half of the spatial frequencies in the initial conditions. The filtered lattice beam, when slightly tilted, can propagate stationarily along the crystal; thus, the Talbot effect is eliminated. Our experimentally created 1D and 2D stationary lattices are presented in Fig. 7.2. A theoretical understanding for the elimination of the Talbot effect by frequency filtering and beam tilting can be found in [63].

In our studies, we need to optically create stationary periodic lattices with a local defect akin to an "air defect" in photonic crystals. To explore this possibility, we prepare an initial periodic lattice with a single-site negative defect using amplitude masks. Under linear propagation, however, we find that the frequency filtering and beam tilting techniques are not enough to maintain the defect and keep the lattice stationary. The defect tends to be washed out at the exit face of the crystal. In order to maintain the defect, we employ two additional techniques. One is to introduce a small amount of nonlinearity

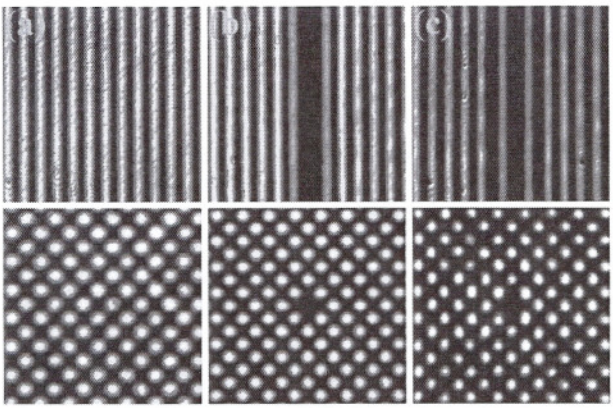

Fig. 7.2. Optically induced 1D and 2D lattices with a single-site negative defect, as obtained from our experiments. 1D results (*top*), 2D results (*bottom*). (**a**) uniform lattice at output, lattice spacing 42 μm (1D) and 27 μm (2D), (**b**) lattice with defect at input, (**c**) lattice with defect at output maintained by weak nonlinearity

into the lattice beam (by setting its polarization to contain a small amount of e-polarized component), and the other one is to introduce partial incoherence into the lattice beam (by letting the lattice beam go through a rotating diffuser). With the combined use of these techniques, we have successfully created 1D and 2D single-site defects in the otherwise uniform lattice which remains nearly stationary throughout the crystal (length varies from 10 to 20 mm). Typical examples are presented in Fig. 7.2.

7.3 Linear Defect Modes in 1D Lattices

When a periodic lattice has a local defect, this defect can affect the propagation of a probe beam significantly and in a way fundamentally different from linear propagation in continuous media. For instance, if the defect is negative (repulsive), i.e., the lattice intensity at the defect is lower than that in neighboring lattice sites, the defect can guide a linear localized mode (defect mode). This is quite counter-intuitive. The physical mechanism for this unusual light guiding is the repeated Bragg reflections, rather than the conventional total internal reflections, analogous to light transmission in air-hole photonic crystal fibers.

To understand the linear light-guiding property of a negative defect, a theoretical analysis is performed first for our present physical system [42,43]. The non-dimensionalized model is [7–9]

$$\mathrm{i}U_z + U_{xx} - \frac{E_0}{1 + I_\mathrm{L}(x)}U = 0\,, \tag{7.1}$$

where U is the envelope function of the probe beam, E_0 is the applied bias field, $I_L(x) = I_0 \cos^2(x)[1 - f_D(x)]$ is the lattice intensity containing a defect, I_0 is the lattice peak intensity, and $f_D(x) = \exp(-x^8/128)$ accounts for the single-site negative defect. If we take $I_0 = 3$, this defective lattice is shown in Fig. 7.3i. A surprising fact is that this negative defect supports localized defect modes (DMs) of the form

$$U(x, z) = u(x)e^{-i\mu z} , \tag{7.2}$$

where μ is the propagation constant (DM eigenvalue). These eigenvalues versus E_0 are shown in Fig. 7.3ii. It is seen that these eigenvalues all lie in the gaps between Bloch bands. None of them exists in the semi-infinite bandgap (total internal reflection region). As E_0 increases, these modes disappear from lower bandgaps, and appear in higher bandgaps. A typical DM profile in the second gap is shown in Fig. 7.3iii. This mode has its intensity maximum inside the negative defect, with double-peaks in each lattice spacing, and its neighboring intensity peaks are out of phase with each other [42, 43].

The above results on DMs are confirmed experimentally, and our experimental results are shown in Fig. 7.3a–d. Here, Fig. 7.3a is the input of the 1D lattice with a defect (lattice spacing about 42 μm), the polarization angle

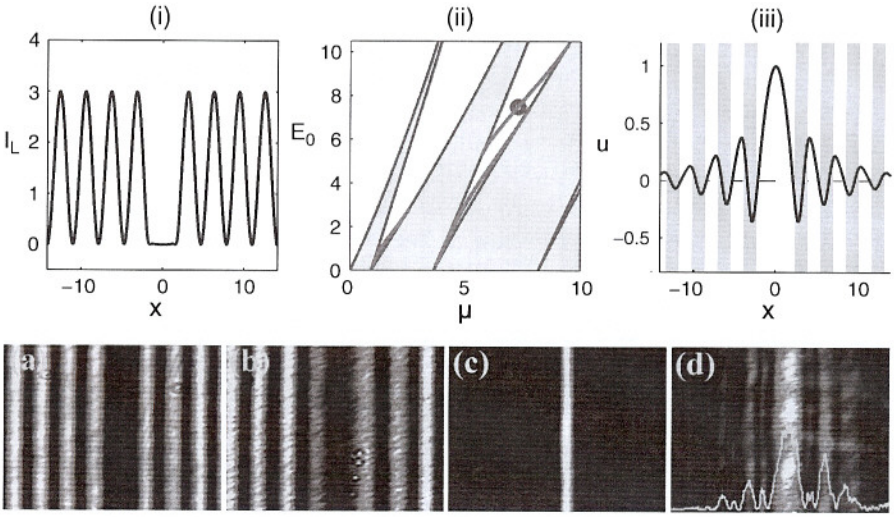

Fig. 7.3. Theoretical demonstration of defect modes (*top*). (**i**) Lattice intensity profile, (**ii**) DM branches in the (μ, E_0) plane, (**iii**) a DM in the second bandgap marked by a circle in (ii). Experimental observation of DMs (*bottom*), shown are transverse intensity patterns of the lattice beam at crystal input (**a**) and output (**b**) with a single-site defect, and those of the probe beam at input (**c**) and output (**b**) after 20 mm propagation through the defect channel. Lattice spacing 42 μm, Bias field 1.1 kV/cm (after Ref. [42, 43, 46])

is about 8% relative to the o-axis, and the propagation distance is 20 mm. At the bias field of 1.1 kV/cm, the output of the lattice is shown in Fig. 7.3b. It is seen that the defect is well maintained throughout propagation. After such a lattice is "fabricated", its light guiding property can be studied. To do so, we launch a low-intensity e-polarized probe beam into the defect. The experimental result is shown in Figs. 7.3c and 7.3d. It can be seen that after 20 mm propagation, most of the probe-beam energy is still confined inside the negative defect. This is remarkable, as without the defect, the probe beam would strongly scatter to nearby lattice sites in case of strong coupling. The experimentally observed defect mode (Fig. 7.3d) closely resembles the theoretical one in Fig. 7.3iii.

7.4 Linear Defect Modes in 2D Square Lattices

Guiding light by defects in 2D periodic lattices is even more interesting. Using experimental techniques similar to those for 1D DMs, we have demonstrated 2D defect guiding as well. The experimental results are shown in Fig. 7.4. Here a 2D lattice with a single-site negative defect is first created in a 20 mm crystal as shown in Fig. 7.2. Then we launch a Gaussian probe beam into the defect (Fig. 7.4a). Under different lattice conditions, we observed different guided structures as shown in Fig. 7.4b–d. At lattice spacing of 27 μm and bias field of 2.8 kV/cm, the Gaussian beam evolves into a DM, with most of its energy concentrated in the defect site (Fig. 7.4b). At spacing 42 μm and bias field of 3.0 kV/cm, the tails along the principal axes of the square lattice (which are diagonally oriented) are more prominent, and they show interesting vortex-array-like structures (Fig. 7.4c). Figure 7.4d shows a typical interferogram corresponding to intensity pattern of Fig. 7.4c, where the locations of vortices are indicated by arrows. It is seen that the vortex cells have different sign of topological charge along two diagonal "tails" [45].

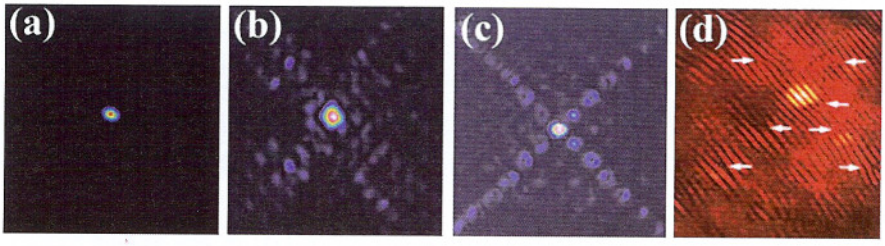

Fig. 7.4. Experimental observations on 2D defect guidance. (**a**) Input probe beam, (**b**), (**c**) intensity patterns of the output probe beam under different lattice conditions, (**d**) zoom-in interferogram of (c) with a tilted plane wave where arrows indicate location of vortices. The brightest spot corresponds to the defect site (after Ref. [45])

To theoretically analyze these various 2D DM structures, we use the 2D model equation

$$\mathrm{i}U_z + U_{xx} + U_{yy} - \frac{E_0}{1 + I_\mathrm{L}(x,y)}U = 0\,, \tag{7.3}$$

where

$$I_\mathrm{L}(x,y) = I_0 \cos^2\left(\frac{x+y}{\sqrt{2}}\right)\cos^2\left(\frac{x-y}{\sqrt{2}}\right)\left\{1 + \varepsilon \exp\left[-\frac{\left(x^2+y^2\right)^8}{128}\right]\right\} \tag{7.4}$$

is the 2D defective lattice, and ε is the defect depth. Localized DMs in the form of $U(x,y,z) = u(x,y)\exp(-\mathrm{i}\mu z)$ are sought for both attractive ($\varepsilon > 0$) and repulsive ($\varepsilon < 0$) defects. We first examine the dependence of defect-modes on the defect strength ε by fixing $E_0 = 15$, $I_0 = 6$, and varying ε from -1 to 1. When the defect is weak, i.e., $\varepsilon \ll 1$, such dependence can be derived analytically by asymptotic methods, and we find that the distance between μ and a Bloch-band edge μ_c decreases exponentially with the defect strength ε, i.e. [48],

$$\mu = \mu_\mathrm{c} + C\mathrm{e}^{-\beta/|\epsilon|}\,, \qquad \varepsilon \ll 1\,, \tag{7.5}$$

where C and $\beta > 0$ are constants. Fig. 7.5 shows the analytical results (dashed lines) as well as our numerical results (solid lines) for both weak and strong defects. When ε is small, they are in very good agreement. Fig. 7.5 also shows that there is one DM branch bifurcating from each band: DMs in an attractive defect ($\varepsilon > 0$) bifurcate from the left edge of each band, and DMs in a repulsive defect ($\varepsilon < 0$) bifurcate from the right edge of each band. As the defect strength ε varies, branches of attractive defect-modes stay inside their respective gaps, while repulsive DM branches march to higher Bloch bands, disappear when reaching the edge of the band, and reappear in higher gaps. Fig. 7.6 shows typical DM profiles corresponding to the letter-marked points in Fig. 7.5. DMs on branches "i", "a" and "b" are symmetric in both x and

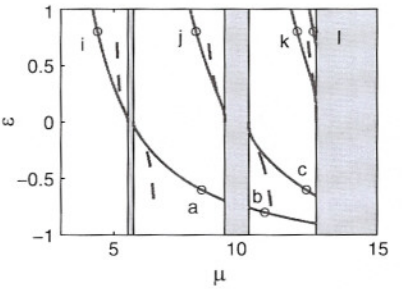

Fig. 7.5. Bifurcation of DMs with the defect lattice (7.4) at $E_0 = 15$ and $I_0 = 6$. Solid lines: numerical results, dashed lines: analytical results. The shaded regions are the Bloch bands. Profiles of defect modes at the circled points are displayed in Fig. 7.6 (after Ref. [48])

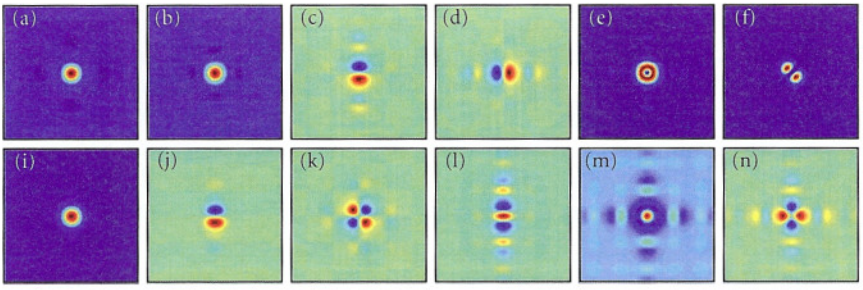

Fig. 7.6. (**a**)-(**c**) and (**i**)-(**l**): profiles of defect modes at the circled points in Fig. 7.5. Repulsive defect modes (*top*), attractive defect modes (*bottom*). (**d**) the co-existing mode of mode (c), (**e**) vortex mode derived from the superposition of mode (c) and (d) with $\pi/2$ phase delay, i.e., in the form of $u(x,y)+\mathrm{i}u(y,x)$, (**f**) dipole mode derived from the superposition of mode (c) and (d) without phase delay, i.e., in the form of $u(x,y)+u(y,x)$, (**m**) and (**n**) modes derived from the superposition of mode (l) and its co-existing mode in the form of $u(x,y)+u(y,x)$ and $u(x,y)-u(y,x)$ respectively (after Ref. [48])

y, with a dominant hump at the defect site, and satisfy the symmetry relation $u(x,y)=u(y,x)$. They can be called fundamental defect modes. DMs on the branches "j" and "c" are dipole-like and do not satisfy the above symmetry relation. Note that there is one branch, i.e., "l", which bifurcates not from a band edge, but rather from an interior point in the third Bloch band. On DM branches with asymmetric modes $u(x,y)$, such as "j", "c" and "l", another linearly independent DM $u(y,x)$ co-exists. For instance, at point "c" in Fig. 7.5, the DM is a dipole along the vertical direction (Fig. 7.6c), while its co-existing DM is a dipole along the horizontal direction (Fig. 7.6d). Due to the linear property of the model equation (7.3), we can get other co-existing DMs by arbitrarily superimposing these two DMs $u(x,y)$ and $u(y,x)$. This linear superposition can produce more interesting DM patterns. For instance, a vortex mode, shown in Fig. 7.6e, can be derived from a superposition of modes "c" and "d" in the form of $u(x,y)+\mathrm{i}u(y,x)$. A dipole mode oriented along the diagonal direction, shown in Fig. 7.6f, can be derived as well by the superposition $u(x,y)+u(y,x)$. Similarly, Fig. 7.6m and 7.6n are derived from the superposition of mode "l" and its co-existing mode in the form of $u(x,y)+u(y,x)$ and $u(x,y)-u(y,x)$, respectively.

Comparing the experimental results of Fig. 7.4 with the theoretical results of Figs. 7.5 and 7.6, we can see that Fig. 7.4b closely resembles a fundamental defect mode of Fig. 7.6b. The tails of vortex arrays in Figs. 7.4c and 7.4d should be related to the vortex DM of Fig. 7.6e when this DM gets close to a Bloch band [45, 64]. Further analysis of tail structures in Figs. 7.4c and 7.4d as well as observations of various DMs in Figs. 7.6 are currently underway.

7.5 Linear Defect Modes in 2D Ring Lattices

Ring-like photonic-lattice structures with a negative defect (a low-index core) are of particular interest as they have direct connections with Bragg fibers and PCFs. Yet it poses a challenge to make such structures by optical induction. Recently, we have succeeded in creating such structures in a *self-defocusing* photorefractive crystal, and subsequently demonstrated defect guiding in 2D ring lattices [44].

The crystal used for this experiment is a 10 mm long SBN:61. The experimental setup is similar to that used for generation of discrete ring lattice solitons reported in [65], except that the Bessel-like lattices [66,67] are induced with a *self-defocusing* nonlinearity, so the center of the lattice is a low index core. With proper filtering, the mask gives rise to a Bessel-like intensity pattern at the crystal input, which remains nearly invariant during propagation throughout the 10 mm long crystal even under a negative bias field of 2 kV/cm (Fig. 7.7A). Starting from the first ring, the measured spacing between adjacent rings in Fig. 7.7A is about 20 μm. We note that the ring pattern created this way is somewhat different from the true Bessel pattern, since the intensity of rings here decreases more slowly (along the radial direction) than in a true Bessel lattice. Under a negative bias field, the crystal has a *self-defocusing* nonlinearity [52,68,69]. This means that the locations of the ring waveguides correspond to the dark (low intensity) areas of the lattice beam, while the center (high-intensity) corresponds to an anti-guide. Thus the ring pattern in Fig. 7.7A induces a periodic ring waveguide lattice with a low-index core.

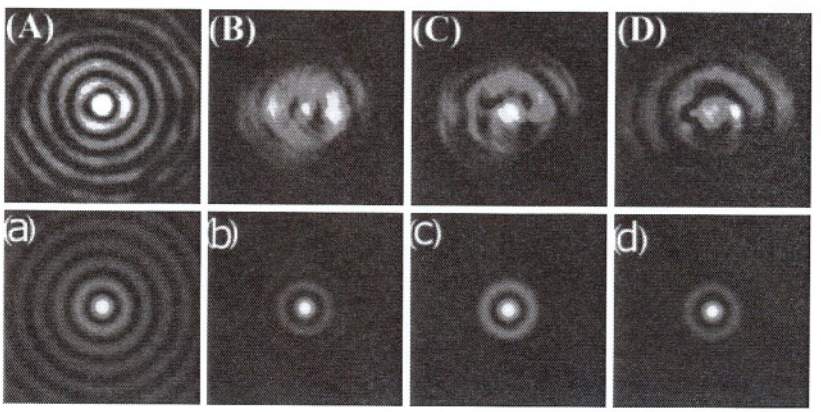

Fig. 7.7. Experimental observation of defect guidance in a ring lattice (*top*). (**A**) a ring lattice (20 μm spacing) established in experiments, (**B**)–(**D**) output of the probe beam in a ring lattice with 37 μm spacing as the negative bias is increased gradually. Theoretical demonstration of quasi-localized defect modes (*bottom*). (**a**) a Bessel-like ring lattice, (**b**) a guided mode in (a), (**c**) the lattice of (a) with outer rings removed, (**d**) a guided mode in (c) (after Ref. [44])

To investigate the waveguiding property in such a ring lattice, a Gaussian-like probe beam (FWHM: 14 μm) is launched directly into the core and propagates collinearly with the lattice. The probe beam is e-polarized but has a wavelength of 632.8 nm that is nearly photo-insensitive for our crystal, so that nonlinear self-action of the probe beam is negligible [52]. Since the index at the center of the lattice is lower than that at its surrounding, the probe beam tends to escape from the center and couple into the surrounding ring waveguides due to evanescent coupling. However, under appropriate conditions, guiding of the probe beam into the core is observed. Typical experimental results are presented in Fig. 7.7B–D for a ring lattice with 37 μm spacing. They show the output patterns of the probe beam as the negative applied dc field is set at three different levels ($-0.6, -1.4$, and -2.0 kV/cm), while the lattice intensity (normalized to background illumination) is fixed. When the bias field is low, the probe beam tends to diffract away from the core (Fig. 7.7B), but as the bias field increases, the probe beam undergoes a transition from discrete diffraction to central guidance (Fig. 7.7C). At even higher bias field, the guidance starts to deteriorate (Fig. 7.7D) because the experimental condition deviates from that for the formation of the defect mode.

To better understand the experimental results in Fig. 7.7, we use the model equation

$$\mathrm{i}U_z + U_{xx} + U_{yy} - \frac{E_0}{1 + I_0|J_0(r)|^{3/2}}U = 0\,, \tag{7.6}$$

where $J_0(r)$ is the Bessel function, and $r = \sqrt{x^2 + y^2}$. Here x and y are normalized by the spacing (pitch) of the lattice far away from the center, and normalizations for I_0, E_0 and z are the same as in [42,43]. The Bessel function $|J_0(r)|^{3/2}$ was chosen for the ring lattice since the first four peaks of this function decay as 1.00, 0.25, 0.16, 0.12, closely resembling those in experiments. Numerical simulations under experimental conditions produce results qualitatively similar to those in Fig. 7.7B–D. Furthermore, we have also searched for guided modes of the above model in the form of $U(x, y, z) = \exp[-\mathrm{i}\mu z]u(r)$ with normalized parameters $E_0 = -15$, and $I_0 = 750$ (corresponding to experimental parameters). At $\mu = 0.97$, we found solutions $u(r)$ which have a high central peak and weak oscillatory tails. One such solution is shown in Fig. 7.7b, which resembles those observed in Fig. 7.7C. Note that in our ring lattice, the intensity decays along the radial direction, and thus bandgaps do not really open in the above model. Thus, the solution in Fig. 7.7b can not be a truly localized defect mode, but has tails decaying very slowly like a Bessel function, and its power is infinite. We can call it a quasi-localized mode. If we keep only the central beam and the first ring of the lattice (see Fig. 7.7c), we find that quasi-localized modes as in Fig. 7.7b persist (see Fig. 7.7d). This finding indicates that the guidance observed in Fig. 7.7C may not be attributed to the repeated Bragg reflections of outer rings, but rather it is dominated by the first high-index ring in our lattice. This guidance seems analogous to that in antiresonant reflecting optical waveguides [70], and certainly merit further

investigation. For instance, one of the subjects in our future research is to see if such low-index core can create any "coloring" effect as that occurred in photonic crystal fibers.

7.6 Nonlinear Defect Modes

In previous sections, we discussed linear DMs and bandgap guidance in different types of photonic lattices containing defects, for which the probe beam propagates in the linear regime. On the other hand, the probe beam can also propagate in the nonlinear regime, where light can also be trapped as localized nonlinear defect modes (defect solitons). This issue has not received much attention before in photonic crystals or PCFs because the nonlinearity there is very weak. In nonlinear waveguide arrays and photonic lattices, however, the nonlinearity is high [1–18]. Thus far, there has been only limited theoretical work on defect solitons in waveguide lattices [41, 47, 51]. In this section, we investigate how nonlinearity affects the formation of 1D defect modes both theoretically and experimentally. The theoretical work is an extension of our earlier results in [47], while the experimental work is new.

We first consider defect solitons in a negative defect under focusing nonlinearity. The experimental setup is similar to the one illustrated in Fig. 7.1. The linear 1D lattice with a single-site negative defect as created in our experiment is shown in Figs. 7.8a and 7.8b. Here the lattice spacing is about 42 μm, the peak intensity (normalized to background illumination) is about 0.65, and the propagation distance is 20 mm. It is seen that the defect is maintained quite well. Next, a probe stripe beam with peak intensity about 0.23 (normalized to background illumination) is launched into this defect. At bias field of 1.1 kV/cm (for self-focusing nonlinearity), the output of linear propagation (taken instantaneously) is shown in Fig. 7.8c. It is seen that the probe beam evolves into a linear defect mode as we have demonstrated in Fig. 7.3d. However, under nonlinear propagation, the output (taken after a steady state has reached) has evolved into a defect soliton shown in Fig. 7.8d. The nonlinear output is similar to the linear output, except that the central stripe is more localized due to self-focusing nonlinearity. These observations demonstrate that defect guiding is quite robust, and sustains under nonlinear effects. This phenomenon is quite different from the nonlinearity-induced escape from defect sites of waveguide arrays as reported in [39].

Theoretically, we employ the model equation similar to (7.1) except that nonlinearity is involved:

$$\mathrm{i}U_z + U_{xx} - \frac{E_0}{1 + I_\mathrm{L}(x) + |U|^2} U = 0 \,. \tag{7.7}$$

Defect soliton solutions of (7.7) are sought in the form of (7.2). Corresponding to experimental conditions, we take $E_0 = 20$, and $I_0 = 0.65$. At these parameter values, the lowest linear defect mode is at $\mu = 20.40$, which lies

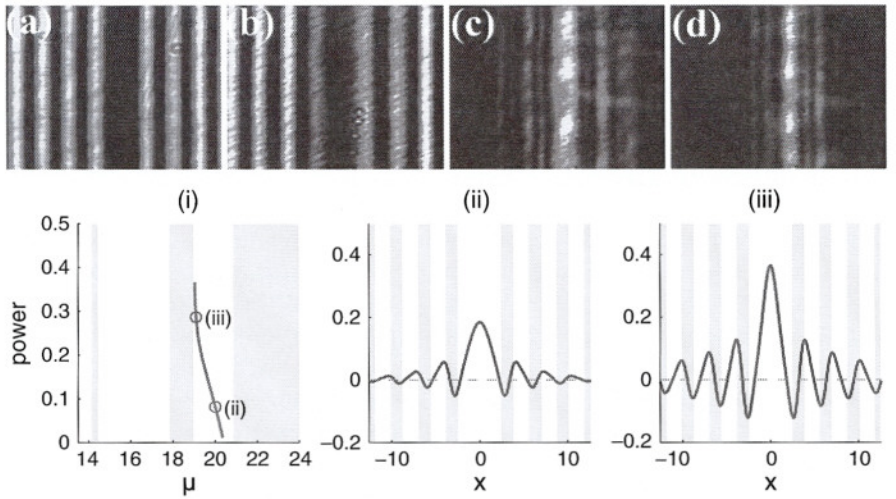

Fig. 7.8. Experimental demonstration of defect solitons in a repulsive defect under focusing nonlinearity (*top*). (**a**) lattice input, (**b**) lattice output, (**c**) probe linear output, (**d**) probe nonlinear output. Theoretical demonstration of defect solitons (*bottom*). (**i**) the power diagram (shaded regions are Bloch bands), (**ii**), (**iii**) profiles of defect solitons at μ values marked by circles in (i). The shaded stripes denote locations of high intensities in the defective lattice

in the second bandgap (between the second and third Bloch bands). Using asymptotic methods, we have shown that bifurcating from every linear defect mode, a family of nonlinear defect solitons will arise [47]. We have computed this family of defect solitons using the modified squared-operator method developed in [71], and its power curve is shown in Fig. 7.8i. We see that at higher powers, this soliton branch moves left toward the lower Bloch band. Two representative mode profiles are displayed in Figs. 7.8ii and 7.8iii. They have symmetric shapes, with peak intensities lying inside the repulsive defect. The profile of Fig. 7.8ii has lower power, and it is very close to the linear defect mode. As the power rises, the central peak becomes narrower (due to nonlinear self-focusing), while the side band mini-peaks become more pronounced (see Fig. 7.8iii). These findings agree well with the experimental observations in Figs. 7.8c and 7.8d.

Next, we present our work on defect solitons in a single-site attractive (rather than repulsive) defect. For this purpose, we only need to turn the nonlinearity from self-focusing to self-defocusing by reversing the sign of the bias field E_0 in the experiment of Fig. 7.8 and in the theoretical model of Eq. (7.7). The question is what types of defect solitons can exist in an attractive defect under self-defocusing nonlinearity. To answer this question, we take $E_0 = -8$, $I_0 = 3$ in Eq. (7.7), and numerically find two families of defect solitons, one in the semi-infinte bandgap, and the other one in the first

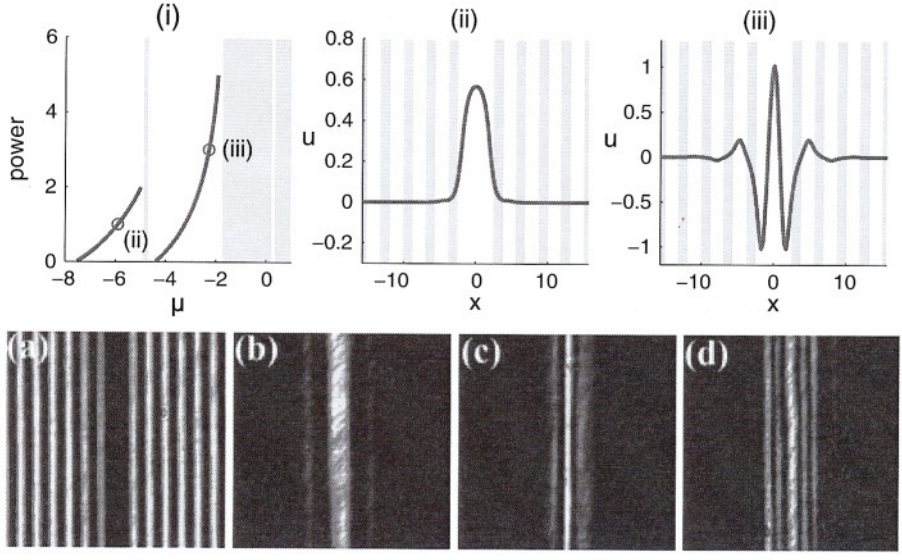

Fig. 7.9. Theoretical demonstration of defect solitons in an attractive defect under defocusing nonlinearity (*top*, $E_0 = -8$, $I_0 = 3$). (**i**) the power diagrams, (**ii**), (**iii**) defect solitons in the semi-infinite and first bandgaps respectively. Experimental observation of defect solitons (*bottom*). (**a**) lattice input, (**b**) defect soliton excited with a single-stripe input at $E_0 = -1.4\,\mathrm{kV/cm}$, corresponding to (ii), (**c**) three-stripe probe input, (**d**) defect soliton excited with (c) at $E_0 = -1.6\,\mathrm{kV/cm}$, corresponding to (iii)

bandgap. The power curves of these families are shown in Fig. 7.9i. We can see that both families bifurcate from the linear defect modes in the low power limit. On the family of the semi-infinite bandgap, a typical soliton profile is shown in Fig. 7.9ii, which consists of a dominant hump inside the defect. Note that this soliton exists under defocusing nonlinearity. It is possible because the negative bias field makes the surrounding lattice sites having lower refractive indices than the center defect, thus due to total internal reflection, such solitons are permitted. For the family in the first bandgap, a typical soliton profile is shown in Fig. 7.9iii. This soliton has three dominant intensity peaks inside the defect site, flanked by weaker peaks nearby. All adjacent peaks are out of phase with each other. This is a higher-order nonlinear defect mode (defect gap soliton) supported by the attractive defect.

Experimentally, these two types of defect solitons under defocusing nonlinearity are also observed. The experimental results are summarized in Fig. 7.9a–d. First, a photonic lattice with a single-site defect is maintained (see Fig. 7.9a). Then we launch a single-stripe probe beam into the defect channel. At bias field of $-1.4\,\mathrm{kV/cm}$, the output of the probe beam is shown in Fig. 7.9b. It can be seen clearly that the probe beam is well guided inside the defect channel despite the fact that a self-defocusing nonlinearity is employed.

This guided mode closely resembles the theoretical defect soliton shown in Fig. 7.9ii. When the input probe beam contains three out-of-phase stripes (Fig. 7.9c), it still remains somewhat localized at the bias field of $-1.6\,\mathrm{kV/cm}$ (Fig. 7.9d). Recalling that such a probe beam would defocus and diverge dramatically should the defect be absent, the formation of such defect gap soliton is again attributed to combined effects of nonlinearity and lattice impurity. When comparing this output with the theoretical solution in Fig. 7.9iii, we see that the outer two peaks in the experiment are more pronounced, but the theoretical and experimental results are in qualitative agreement. These studies of nonlinear defect modes and defect gap solitons can readily be extended to the 2D domain.

7.7 Summary

In summary, we have successfully fabricated 1D and 2D defective photonic lattices by the method of amplitude modulation together with several other techniques such as frequency filtering, partial spatial coherence, and polarization-controlled index variation. We have also studied light guiding in these defective lattices, and shown that these defects can guide a wide array of defect modes in both linear and nonlinear regimes. Our results pave the way for further studies of new phenomena in photonic structures with built-in defects, as well as for exploring potential applications in beam shaping and light routing with reconfigurable lattices. Since defects exist in a wide array of other periodic linear and nonlinear systems, our work may prove to be relevant to the studies of defect-mediated phenomena in other branches of physics and nonlinear sciences.

Acknowledgements

This work was supported in part by NSF, AFOSR, and the 973 program.

References

1. D.N. Christodoulides, F. Lederer, and Y. Siberberg, Nature **424**, 817 (2003)
2. Y.S. Kivshar and G.P. Agrawal, *Optical solitons*, Academic Press, New York (2003)
3. D. Campbell, S. Flach, and Y.S. Kivshar, Phys. Today **57**, 43 (2004)
4. D.N. Christodoulides and R.I. Joseph, Opt. Lett. **13**, 794 (1988)
5. H.S. Eisenberg, Y. Silberberg, R. Morandotti, A.R. Boyd, and J.S. Aitchison, Phys. Rev. Lett. **81**, 3383 (1998)
6. R. Morandotti, H.S. Eisenberg, Y. Silberberg, M. Sorel, and J.S. Aitchison, Phys. Rev. Lett. **86**, 3296 (2001)
7. N.K. Efremidis, S. Sears, D.N. Christodoulides, J.W. Fleischer, and M. Segev, Phys. Rev. E **66**, 046602 (2002)

8. J.W. Fleischer, T. Carmon, M. Segev, N.K. Efremidis, and D.N. Christodoulides, Phys. Rev. Lett. **90**, 023902 (2003)
9. J.W. Fleischer, M. Segev, N.K. Efremidis, and D.N. Christodoulides, Nature **422**, 147 (2003)
10. D. Neshev, E. Ostrovskaya, Y. Kivshar, and W. Krolikowski, Opt. Lett. **28**, 710 (2003)
11. H. Martin, E.D. Eugenieva, Z. Chen, and D.N. Christodoulides, Phys. Rev. Lett. **92**, 123902 (2004)
12. Z. Chen, H. Martin, E.D. Eugenieva, J. Xu, and A. Bezryadina, Phys. Rev. Lett. **92**, 143902 (2004)
13. B.A. Malomed and P. G. Kevrekidis, Phys. Rev. E **64**, 026601 (2001)
14. J. Yang and Z. H. Musslimani, Opt. Lett. **28**, 2094 (2003)
15. Z. Musslimani and J. Yang, J. Opt. Soc. Am. B **21**, 973 (2004)
16. J. Yang, New Journal of Physics **6**, 47 (2004)
17. D.N. Neshev, T.J. Alexander, E.A. Ostrovskaya, Y.S. Kivshar, H. Martin, I. Makasyuk, and Z. Chen, Phys. Rev. Lett. **92**, 123903 (2004)
18. J.W. Fleischer, G. Bartal, O. Cohen, O. Manela, M. Segev, J. Hudock, and D.N. Christodoulides, Phys. Rev. Lett. **92**, 123904 (2004)
19. R. Iwanow, R. Schiek, G.I. Stegeman, T. Pertsch, F. Lederer, Y. Min, W. Sohler, Phys. Rev. Lett. **93**, 113902 (2004)
20. T. Pertsch, U. Peshchl, J. Kobelke, K. Schuster, H. Bartelt, S. Nolte, A. Tünnermann, and F. Lederer, Phys. Rev. Lett. **93**, 053901 (2004)
21. A. Fratalocchi, G. Assanto, K.A. Brzdakiewicz, and M.A. Karpierz, Opt. Lett. **29**, 1530 (2004)
22. Y.S. Kivshar, Opt. Lett. **18**, 1147 (1993)
23. D. Mandelik, R. Morandotti, J.S. Aitchison, and Y. Silberberg, Phys. Rev. Lett. **92**, 093904 (2004)
24. D. Neshev, A.A. Sukhorukov, B. Hanna, W. Krolikowski, and Y.S. Kivshar, Phys. Rev. Lett. **93**, 083905 (2004)
25. F. Chen, M. Stepic, C. Rter, D. Runde, D. Kip, V. Shandarov, O. Manela, and M. Segev, Opt. Express **13**, 4314 (2005)
26. C. Lou, X. Wang, J. Xu, Z. Chen, and J. Yang, Phys. Rev. Lett. **98**, 213903 (2007)
27. J.D. Joannopoulos, R.D. Meade, J.N. Winn, *Photonic Crystals: Molding the Flow of Light*, Princeton University Press, New Jersey (1995)
28. P. Russell, Science **299**, 358 (2003)
29. S.L. McCall, P.M. Platzman, R. Dalichaouch, D. Smith, and S. Schultz, Phys. Rev. Lett. **67**, 2017 (1991)
30. E. Yablonovitch, T.J. Gmitter, R.D. Meade, A.M. Rappe, K.D. Brommer, and J.D. Joannopoulos, Phys. Rev. Lett. **67**, 3380 (1991)
31. M. Bayindir, B. Temelkuran, and E. Ozbay, Phys. Rev. Lett. **84**, 2140 (2000)
32. F. Luan, A.K. George, T.D. Hedley, G.J. Pearce, D.M. Bird, J.C. Knight, and P.St.J. Russell, Opt. Lett. **29**, 2369 (2004)
33. A. Argyros, T.A. Birks, S.G. Leon-Saval, C.B. Cordeiro, F. Luan, and P.St.J. Russell, Opt. Express **13**, 309 (2005)
34. J. Schmidtke, W. Stille, and H. Finkelmann, Phys. Rev. Lett. **90**, 083902 (2003)
35. J.S. Foresi, P.R. Villeneuve, J. Ferrera, E.R. Thoen, G. Steinmeyer, S. Fan, J.D. Joannopoulos, L.C. Kimerling, H.I. Smith, and E.P. Ippen, Nature **390**, 143 (1997)

36. S. Fan, P.R. Villeneuve, J.D. Joannopoulos, and H.A. Haus, Phys. Rev. Lett. **80**, 960 (1998)
37. X. Wu, A. Yamilov, X. Liu, S. Li, V.P. Dravid, R.P.H. Chang, and H. Cao, Appl. Phys. Lett. **85**, 3657 (2004)
38. O. Painter, R.K. Lee, A. Scherer, A. Yariv, J.D. O'Brien, P.D. Dapkus, and I. Kim, Science **284**, 1819 (1999)
39. U. Peschel, R. Morandotti, J.S. Aitchison, H.S. Eisenberg, and Y. Silberberg, Appl. Phys. Lett. **75**, 1348 (1999)
40. R. Morandotti, H.S. Eisenberg, D. Mandelik, Y. Silberberg, D. Modotto, M. Sorel, C.R. Stanley, and J.S. Aitchison, Opt. Lett. **28**, 834 (2003)
41. A.A. Sukhorukov and Y.S. Kivshar, Phys. Rev. Lett. **87**, 083901 (2001)
42. F. Fedele, J. Yang, and Z. Chen, Opt. Lett. **30**, 1506 (2005)
43. F. Fedele, J. Yang, and Z. Chen, Stud. Appl. Math. **115**, 279 (2005)
44. X. Wang, Z. Chen and J. Yang, Opt. Lett. **31**, 1887 (2006)
45. I. Makasyuk, Z. Chen and J. Yang, Phys. Rev. Lett. **96**, 223903 (2006)
46. X. Wang, J. Yang, Z. Chen, D. Weinstein, and J. Yang, Opt. Express **14**, 7362 (2006)
47. J. Yang and Z. Chen, Phys. Rev. E **73**, 026609 (2006)
48. J. Wang, J. Yang, and Z. Chen, Phys. Rev. A **76**, 013828 (2007)
49. G. Bartal, O. Cohen, H. Buljan, J.W. Fleischer, O. Manela, and M. Segev, Phys. Rev. Lett. **94**, 163902 (2005)
50. B. Freedman, R. Lifshitz, J.W. Fleischer, and M. Segev, Nature **440**, 1166 (2006)
51. M.J. Ablowitz, B. Ilan, E. Schonbrun, and R. Piestun, Phys. Rev. E **74**, 035601 (2006)
52. M. Shih, Z. Chen, M. Mitchell, and M. Segev, J. Opt. Soc. Am. B **14**, 3091 (1997)
53. M. Mitchell, Z. Chen, M. Shih, and M. Segev, Phys. Rev. Lett. **77**, 490 (1996)
54. Z. Chen, M. Mitchell, M. Segev, T.H. Coskun, and D.N. Christodoulides, Science **280**, 889 (1998)
55. Z. Chen, M. Segev, and D.N. Christodoulides, J. Opt. A **5**, S389 (2003)
56. Z. Chen and K. McCarthy, Opt. Lett. **27**, 2019 (2002)
57. Z. Chen, K. McCarthy, and H. Martin, Optics and Photonic News, December 2002
58. J. Petter, J. Schröder, D. Träger, and C. Denz, Opt. Lett. **28**, 438 (2003)
59. M. Petrovic, D. Träger, A. Strinic, M. Belic, J. Schröder, and C. Denz, Phys. Rev. E **68**, 055601 (2003)
60. D.N. Neshev, Y.S. Kivshar, H. Martin, and Z. Chen, Opt. Lett. **29**, 486 (2004)
61. H.F. Talbot, Philos. Mag. **9**, 401 (1836)
62. R. Iwanow, D.A. May-Arrioja, D.N. Christodoulides, G.I. Stegeman, Y. Min, and W. Sohler, Phys. Rev. Lett. **95**, 053902 (2005)
63. Z. Chen and J. Yang, "Controlling light in reconfigurable photonic lattices", chapter in H.A. Abdeldayem and D.O. Frazier (ed.), *Nonlinear Optics and Applications*, pp. 103–150, Research Signpost, Kerala, India (2007)
64. Z. Shi and J. Yang, Phys. Rev. E **75**, 056602 (2007)
65. X. Wang, Z. Chen, and P.G. Kevrekidis, Phys. Rev. Lett. **96**, 083904 (2006)
66. Y.V. Kartashov, V.A. Vysloukh, and L. Torner, Phys. Rev. Lett. **93**, 093904 (2004)
67. Z. Xu, Y.V. Kartashov, L. Torner, and V.A. Vysloukh, Opt. Lett. **30**, 1180 (2005)

68. Z. Chen, H. Martin, A. Bezryadina, D. Neshev, Y.S. Kivshar, and D.N. Christodoulides, J. Opt. Soc. Am. B **22**, 1395 (2005)
69. Z. Chen, H. Martin, E.D. Eugenieva, J. Xu, J. Yang, and D.N. Christodoulides, Opt. Express **13**, 1816 (2005)
70. N.M. Litchinitser, A.K. Abeeluck, C. Headley, and B.J. Eggleton, Opt. Lett. **27**, 1592 (2002)
71. J. Yang and T.I. Lakoba, Stud. Appl. Math. **118**, 153 (2007)